Photoluminescence properties and Raman analysis of Sn doped nanostructure ZnO synthesized by the anneal route

NING YANG[a], JUN ZENG[b,*], JUN XUE[b], SHIQUAN ZHANG[b], LINGKUN ZENG[b], YAO ZHAO[b]
[a]*School of Automation, Northwestern Polytechnical University, Xi'an 710072, P. R. China*
[b]*School of Science, Engineering University of PAP, Xi'an 710086, P. R. China*

This work reports that Sn doped ZnO nanostructures (NZSs) were synthesized by annealing ZnSn alloys at different temperature for 4 hours in air. ZnSn alloys were prepared by the powder metallurgy route. The structure and optical properties were characterized by X-ray diffraction (XRD), micro-Raman scattering technology, field emission scanning electron microscope (FESEM) and photoluminescence (PL) spectrum. The result of mutli-peak Gaussian fitting showed that the blue shift was more pronounced with the increasing annealing temperature, indicating that the Sn doped ZnO were obtained. The nanofiber-like NZSs showed the strongest UV emission peaks. The possible growth mechanism of the NZSs was discussed.

(Received November 14, 2016; accepted October 10, 2017)

Keywords: Nanostructures, Crystal growth, Doped Powder metallurgy, Photoluminescence

1. Introduction

Because of the wide band gap (~3.37 eV) of Zinc oxide (ZnO) at room temperature and large exciton binding energy (~60 meV) [1], ZnO was widely recognized as an ideal material for the application in exciton-related optoelectronic devices. In this regard, ZnO was an important oxide semiconductor with interesting electrical, optical and mechanical properties and have been studied for bioimaging, LED power enhancement and many other applications [2-4]. Additionally, ZnSnO has recently emerged as a promising candidate for optoelectronic devices and gas sensors due to its large optical band gap (~3.6 eV) [5], resulting in high transmittance from the UV to the infrared regime, and its conductivity dependence on the environment. Previous techniques have been developed for synthesizing ZnO and ZnSnO nanostructure, including electrochemical deposition [6], solid-vapor deposition [7], thermal evaporation [8], metal-organic chemical vapor deposition [9] and aqueous solution method [10]. Additionally, Ilican et al. [11] reported that Sn doping effects on the electro-optical properties of sol gel derived transparent ZnO films. Sheini et al. [12] reported low temperature growth of aligned ZnO nanowires and their application as field emission cathodes. Lan et al. [13] reported that string-like ZnO/SnO nanowire/nanosheet nano-heterostructures were synthesized by a two-stage vapor transport and condensation method. Medwal et al. [14] reported the observation of coherent phonon modes in zinc oxide nanostructures synthesized by arc exploding technique (AET). Kumar et al. [15] reported that the correlation between structural and optical properties of nanocrystalline ZnO synthesized by the citrate precursor method had been investigated. Bayan et al. [16] reported that chemically grown SnO coated ZnO nanoneedles were used for modifying light emission and detection features. Recently, the metal doped zinc oxide nanoparticles synthesized by different route were broadly reported [17-22]. In this paper, we reported that the NZSs were prepared by annealing the ZnSn alloys synthesized by powder metallurgy route.

2. Experiments

Zinc powder (Zn, analytical reagent), tin powder (Sn, analytical reagent) were purchased from Beijing Mountain Technical Development Center Co. Ltd (Beijing, China). ZnSn alloys were prepared by powder metallurgy route. The route involves three steps: (1) Zinc and tin powders (1:1 in weight ratio) were well-mixed in the mortar for 1 hours; (2) the mixtures of two metals were pressed into sheets (the volume, 55 mm × 10 mm × 3 mm) at 350 Mpa for 10 minutes; and (3) the sheets were sintered at 400 ^{o}C for 2 hours, and argon was used as protection gas during sintering. After cooled down naturally to room temperature, ZnSn alloys were obtained.

NZSs were synthesized by thermal oxidation route.

ZnSn alloys were annealed at 500 °C, 600 °C, and 700 °C for 4 hours in air, respectively. The heating rate was about 10°C/min. After cooled down naturally to room temperature, NZSs were obtained. In order to investigate the structure and the morphology, NZSs were characterized by X-ray diffraction (XRD, X′ per pro), micro-Raman scattering (Horiba Job RAM HR 800 UV-vis μ- Raman) and field emission scanning electron microscope (FE-S4800). In this work, XRD measurements were carried out using Cu Kα radiation (λ=1.54056 nm) from a sealed tube operated at 45 kV and 40 mA. The crystallite size was calculated from Scherer's equation: $D = \frac{K_w \lambda}{FWHM \cos\theta}$, Where D was the mean crystallite size, K_w was a dimensionless number [16], λ was the X-ray wavelength, FWHM was the full width half maximum intensity and θ was the Bragg diffraction angle. Raman spectra were measured at room temperature with a JY-HR 800 UV Raman spectroscope working at the 325 nm laser line and on different regions of the samples. Photoluminescence (PL) measurements were carried out at room temperature using a RF-5301 system. A He–Cd laser with a wavelength of 325nm was used as the excitation source.

3. Results and discussions

Fig. 1 showed the XRD patterns of ZnSn alloys, pure ZnO and NZSs synthesized at 500 °C, 600 °C, and 700 °C in air, respectively. The results showed that the NZSs were obtained by annealing ZnSn alloys at different temperatures. The diffraction peaks could be indexed according to ZnO with wurtzite structure (JCPDS No. 36-1451). It should be noticed that (101) diffraction peak was the dominant peak, indicating that the preferential growth direction of ZnO was (101) preferred orientation. Additionally, SnO (JCPDS No. 24-1342), Zn (JCPDS No. 04-0831) and Sn (JCPDS No. 04-0673) phases were observed. The XRD patterns of NZSs shifted to higher angles in different peak positions when compared with pure ZnO and NZSs, respectively. This was ascribed to the Sn ions substitutes for the Zn ions. The results indicate that c-axis lattice constant decreases when Sn ions incorporate into ZnO lattice by occupying the Zn sites.

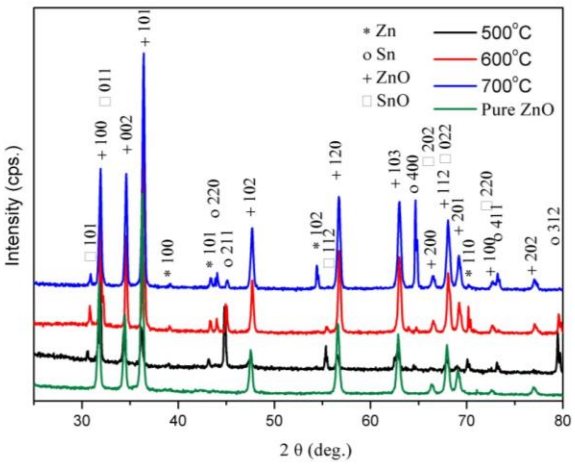

Fig. 1. XRD patterns of NZSs and pure ZnO

Wurtzite-phase ZnO belongs to the space group C_{6v}^4 with two formula units per primitive cell. There were eight zone-center optical-phonon modes $2A_1 + 2B_1 + 2E_1 + 2E_2$, four of which $A_1 + E_1 + 2E_2$ were Raman active [23]. One A_1 and E_1 modes were acoustic phonons and the remaining modes were optical phonons. In the optical phonons, A_1 and E_1 were polar modes, B_1 was a silent mode and E_2 was a non-polar mode [24]. Fig. 2 showed the micro-Raman scattering spectra of synthesized NZSs at different temperature in the range of 100 - 2000 cm^{-1}. The results showed that there were three Raman peaks at 574 cm^{-1}, 1156 cm^{-1}, and 1739 cm^{-1}. In comparison with the vibration spectra of a ZnO single crystal, we could assign the peak at 574cm^{-1} to the A_1 mode, the peak at 1156 cm^{-1} to E_1 mode and the peaks at 1739 cm^{-1} to the E_2 modes. In previous report, Ting et al. [25] reported that the Raman peaks of ZnO nanorods were at 580 cm^{-1}, 1150 cm^{-1} and 1720 cm^{-1}, respectively. Medwal et al. [14] reported that the Raman peaks of ZnO nanorods were at 574 cm^{-1}, respectively. The peak at 574 cm^{-1} was attributed to the surface oxidation of Zn nanoparticles resulting in ZnO at Zn core shell structure. In this work, the Raman peaks at 1156 cm^{-1} and 1739 cm^{-1} were shifted slightly and weaken with the annealing temperature increasing, indicating that the Sn doped ZnO were obtained. The results were consistent with the XRD results.

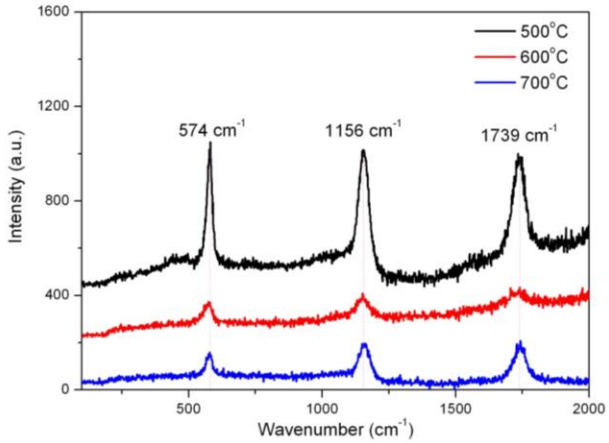

Fig. 2. Micro-Raman scattering spectra of NZSs synthesized by annealing the ZnSn alloys at 500 °C, 600 °C, and 700 °C, respectively

Fig. 3 showed the different magnification FESEM images of NZSs synthesized by annealing the ZnSn alloys at 500 °C, 600 °C, and 700 °C for 4 hours in air, respectively. The results show that the different shapes of NZSs were exhibited after SnZn alloys annealed at different temperatures. The diameter of NZSs increased with the anneal temperature increasing. A large number of nanorod-like NZSs were obtained after SnZn annealed at 500 °C, and the diameter and length of nanofibers were about 40 nm and 800 nm, respectively (Fig. 3a and b). The nanofiber-like NZSs were obtained after SnZn annealed at 600 °C, and the diameter and length of nanofibers were about 50 nm and 60 μm, respectively (Fig. 3c and d). The needle-like Sn doped ZnO microstructures were obtained after SnZn annealed at 700 °C, and the diameter and length of the microneedles were about 2μm and 10μm, respectively (Fig. 3e and f). During the thermal oxidation process, with the annealing temperature increasing, tin first melt to liquid, and then zinc grains were coated by liquid tin. Parts of tin were oxidized first on the thin film surface of the grains, and then the oxidation grew into inner tin films and zinc grains. Due to the different thermal expansion coefficient of tin films and zinc grains and the volume expansion effect of the combination of Zn and O, the internal stress was accumulated in the interface between tin films and Zinc grains, and the compress stress was induced in oxide layer. When the annealing temperature was raised to 500 °C, the energy was released and the nanorod-like NZSs were obtained. When the annealing temperature was raised to 700 °C, much energy accumulated. So the much energy was released, and the larger numbers of Sn doped ZnO microneedles were obtained. It could be concluded that the growth of NZSs was as a result of the accumulation and the relaxation of the internal stress. Additionally, other tiny tin droplets (white ring marked) were used as the catalyst giving a favorable growth orientation, and NZSs were obtained (Fig. 3b). With the annealing temperature increasing from 500 °C to 700 °C, the diameter and length of NZS acutely increase. The nanorod-like NZSs became into nanowire-like and microneedles. This process was achieved by the atomic diffusion [26, 27]. Therefore, the growth mechanism of the present NZSs was related to vapor-liquid-solid mechanism (VLS) and the relaxation of the internal stress. Further investigation of its growth mechanism was still needed.

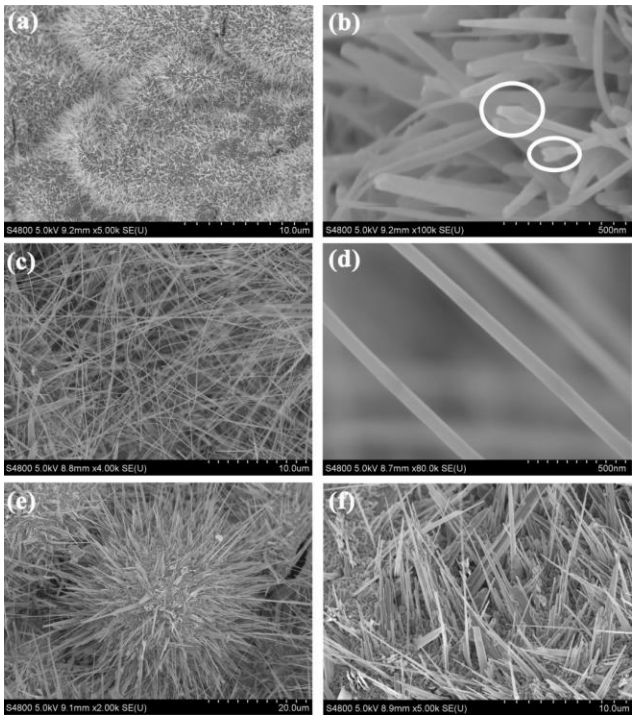

Fig. 3. The different magnification FESEM photographs of NZSs synthesized by annealing the ZnSn alloys at different temperature, respectively. (a and b) annealing at 500 °C; (c and d) annealing at 600 °C; (e and f) annealing at 700 °C

Room temperature photoluminescence (PL) spectra were recorded to evaluate the optical properties of NZSs, which were measured with an excitation wavelength of 325 nm at room temperature. Fig. 4 showed the PL spectra of NZSs synthesized by annealing the ZnSn alloys at 500 °C, 600 °C, and 700 °C for 4 hours in air, respectively. The results showed two broad emission peaks covering the range from 370 to 420 nm and 420 to 630 nm, respectively. The emission peaks blue shift and intensity reduction were more pronounced with the increasing annealing temperature. The nanofiber-like NZSs showed the strongest UV emission peaks. In order to further investigate the optical properties of NZSs, Fig. 5 showed the multi-peak Gaussian fitting PL spectra of the samples synthesized at different temperature. The results showed that the broad emission peaks were well fitted by five peaks, respectively. When the NZSs were synthesized at

500°C, the center of five Gaussian fitting peaks were at 384, 402, 481, 534, and 604 nm, respectively. When the preparation temperature of NZSs was raised to 600°C, the center of five Gaussian fitting peaks were shifted to 389, 407, 477, 532, and 617 nm, respectively. With the annealing temperature increasing to 700°C, the center of five Gaussian fitting peaks were shifted to 387, 403, 475, 522, and 608 nm, respectively. The near-band-edge UV emission peaks at 384, 389, and 387nm indicated the radiative emission involving the shallow trap states lying [28]. The prominent peaks at 402, 407, 403 nm corresponded to the emission due to neutral and ionized zinc vacancydefects [29]. The blue-green emission peaks at 475, 477, and 481 nm from pure ZnO nanoparticle was due to a transition of a photogenerated electron from the conduction band to deeply trapped O^{2-}/O^{-} ion at the surface [30]. The green-yellow emission peaks at 522, 532, and 534 nm were dependent of oxygen vacancies, oxygen interstitials, zinc vacancies and zinc interstitials [31-34]. In this work, the intensity of green-yellow emission peaks increased and blue shifted, because zinc interstitials increased with the annealing temperature increasing. It was consistent with the XRD results. Additionally, we considered that the orange-red emission peaks at 604, 608, and 617 nm were resulted from the interstitial tin of NZSs. It was possible that the tin would introduce inner defects. In this paper, the NZSs were synthesized by annealing ZnSn alloys at different temperature for 4 hours in air. ZnSn alloys were prepared by the powder metallurgy route. Inevitably, the growth process of NZSs introduced above would result in different internal defects, such as distortion of lattice, Sn ions and interstitial tin. Therefore, red, yellow, green emissions were observed. It was possibly ascribed to surface defects and different morphology. However, the detailed mechanism of the PL properties needs further in-depth researched.

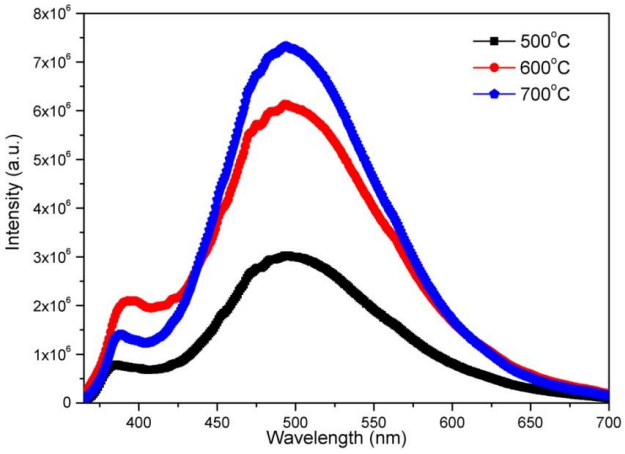

Fig. 4. The room temperature PL spectra of the NZSs synthesized by annealing the ZnSn alloys at 500 °C, 600 °C, and 700 °C, respectively

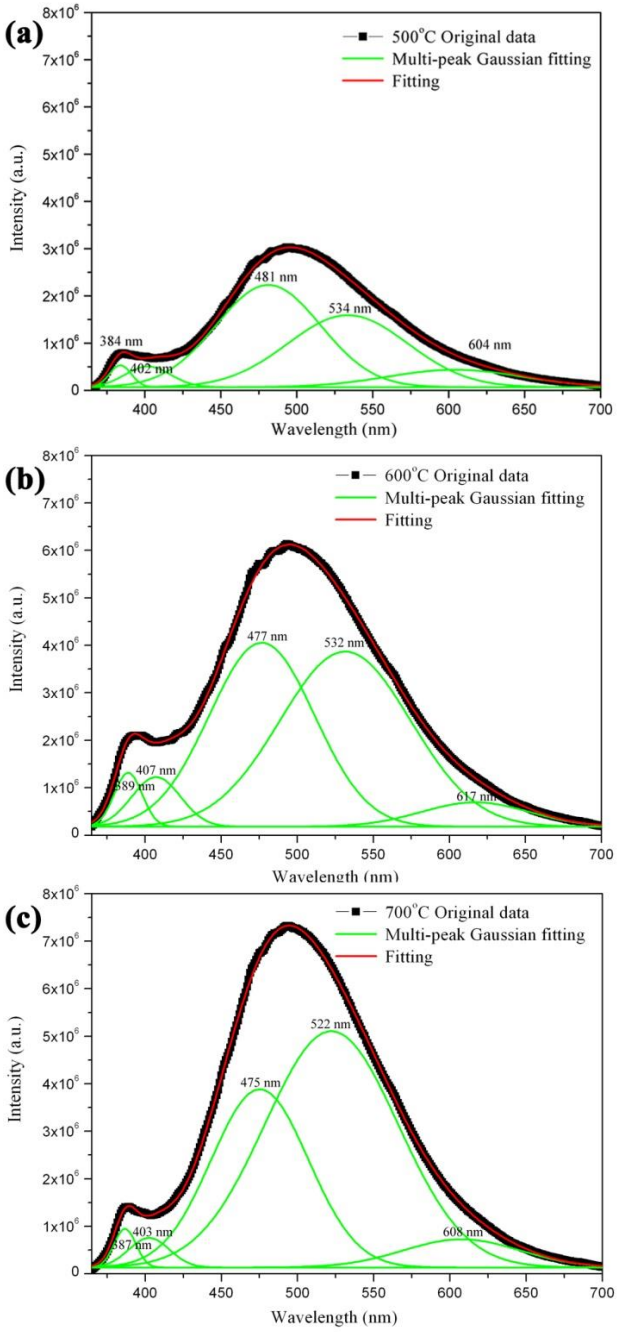

Fig. 5. The room temperature multi-peak Gaussian fitting PL spectra of the NZSs synthesized by annealing the ZnSn alloys at different temperature, respectively. (a) 500 °C, (b) 600 °C, and (c) 700 °C

4. Conclusion

The NZSs were prepared by annealing the ZnSn alloys synthesized by powder metallurgy route. The XRD and Raman spectra indicated that the Sn ions were doped into ZnO. The multi-peak Gaussian fitting PL spectra of NZSs showed that the broad emission peaks were well fitted by five peaks. The emission peaks blue shift and intensity reduction were more pronounced with the

increasing annealing temperature. The nanofiber-like NZSs showed the strongest UV emission peaks. The growth mechanism of the present NZSs was related to vapor-liquid-solid mechanism and the relaxation of the internal stress.

Acknowledgement

This work was supported by the National Natural Science Foundation of China (51302318 and 61771490), the Province Natural Science Foundation of Shan Xi (2011JQ6013) and the basic research foundation of Engineering University of PAP (WJY-201406).

References

[1] C. Klingshirn, Phys. Status solidi B **71**(2), 547 (1975).
[2] C. Zhou, Y. Geng, Q. Chen, J. Xu, N. Huang, Y. Gan, L. Zhou, Mater. Lett. **172**, 171 (2016).
[3] Z. Zang, X. Tang, J. Alloy. Compd. **619**, 98 (2015).
[4] Z. Zang, X. Zeng, J. Du, M. Wang, X. Tang, Opt. Lett. **41**(15), 3463 (2016).
[5] D. L. Young, H. Moutinho, Y. Yan, T. J. Coutts, J. Appl. Phys. **92**(1), 310 (2002).
[6] F. J. Sheini, I. S. Mulla, D. S. Joag, M. A. More, Thin Solid Films **517**(24), 6605 (2009).
[7] X. D. Wang, Y. Ding, C. J. Summer, Z. L. Wang, J Phys. Chem. B **108**(26), 8773 (2004).
[8] X. Wang, Q. W. Li, Z. B. Liu, J. Zhang, Z. F. Liu, R. M. Wang, Appl. Phys. Lett. **84**(24), 4941 (2004).
[9] D. J. Lee, J. Y. Park, Y. S. Yun, Y. S. Hong, J. H. Moon, B. T. Lee, S. S. Kim, J. Cryst. Growth **276**(3-4), 458 (2005).
[10] Y. Tak, K. J. Yong, J. Phys. Chem. B **109**(41), 19263 (2005).
[11] S. Ilican, M. Caglar, Y. Caglar, Appl. Surf. Sci. **256**(23), 7204 (2010).
[12] F. J. Sheini, D. S. Joag, M. A. More, J. Singh, O. N. Srivasatva, Mater. Chem. Phys. **120**(2-3), 691 (2010).
[13] C. Y. Lan, J. F. Gong, Y. W. Jiang, J. Alloy Compd. **575**, 24 (2013).
[14] R. Medwal, S. Gupta, S. P. Pavunny, R. K. Katiyar, S. Annapoorni, R. S. Katiyar, Mater. Lett. **160**, 183 (2015).
[15] V. Kumar, S. Kumari, P. Kumar, M. Kar, L. Kumar, Adv. Mater. Lett. **6**(2), 139 (2015).
[16] S. Bayan, S. K. Mishra, B. Satpati, R. K. Srivastava, R. K. Shukla, P. Chakraborty, J. Vac. Sci. Technol. B **34**(6), 061201 (2016).
[17] Y. Su, L. Li, Y. Chen, Q. Zhou, M. Gao. Q. Chen, Y. Feng, J. Cryst. Growth **311**(8), 2466 (2009).
[18] F. J. Sheini, D. S. Joag, M. A. More, Thin Solid Films **519**(1), 184 (2010).
[19] S. O. B. Oppong, W. W. Anku, S. K. Shukla, P. P. Govender, Res. Chem. Intermed. **42**, 8 (2016).
[20] R. Abaira, E. Buffagni, A. Matoussi, H. Khmakhem, C. Ferrari, Superlattice. Microst. **86**, 438 (2015).
[21] S. Suresh, S. Karthikeyan, J. Iran. Chem. Soc. **13**(11), 2049 (2016).
[22] E. Mosquera, C. R. Michea, M. Morel, F. Gracia, V. Fuenzalida, R. A. Zárate, Appl. Surf. Sci. **347**, 561 (2015).
[23] L. L. Yang, J. H. Yang, D. D. Wang, Y. J. Zhang, Y. X. Wang, H. L. Liu, H. G Fan, J. H. Lang, Phys. E **40**(4), 920 (2008).
[24] J. Kennedy, B. Sundrakannan, R. S. Katiyar, A. Markwitz, Z. Li, W. Gao, Curr. Appl. Phys. **8**(3-4), 291 (2008).
[25] J. M. Ting, K. H. Liao, T. L. Chou, Thin Solid Films **515**(12), 5123 (2007).
[26] J. T. Chen, F. Zhang, J. Wang, G A. Zhang, B. B. Miao, X. Y. Fan, D. Yan, P. X. Yan, J. Alloy Compd. **454**(1-2), 268 (2008).
[27] S. Ren, Y. F. Bai, J. Chen, S. Z. Deng, N. S. Xu, Q. B. Wu, S. Yang, Mater. Lett. **61**(3), 666 (2007).
[28] Y. S. Wang, P. J. Thomas, P. O. Brien, J. Phys. Chem. B **110**(9), 4099 (2006).
[29] S. Bayan, P. Chakraborty, Appl. Surf. Sci. **303**, 233 (2014).
[30] A. V. Dijken, E. A. Meulenkamp, D. Vanmaekelbergh, A. Meijerink, J. Lumin. **87-89**, 454 (2000).
[31] D. Li, Y. H. Leung, A. B. Djurisic, Z. T. Liu, M. H. Xie, S. L. Shi, S. J. Xu, W. K. Chan, Appl. Phys. Lett. **85**(9), 1601 (2004).
[32] N. H. Alvi, S. M. U. Ali, S. Hussain, O. Nur, M. Willander, Scripta Mater. **64**(8), 697 (2011).
[33] N. S. Norberg, D. R. Gamelin, J. Phys. Chem. B **109**(44), 20810 (2005).
[34] A. B. Djurisic, Y. H. Leung, K. H. Tam, L. Ding, W. K. Ge, H. Y. Chen, S. Gwo, Appl. Phys. Lett. **88**(10), 103107 (2006).

*Corresponding author: zengjun2006@gmail.com